Journal of Fluids and Structures (1999) **13,** 225–249
Article No.: jfls.1998.0201, available online at http://www.idealibrary.com on IDEAL

NUMERICAL PREDICTION OF FORCE ON RECTANGULAR CYLINDERS IN OSCILLATING VISCOUS FLOW

W. ZHENG* AND C. DALTON

Department of Mechanical Engineering, University of Houston, Houston, TX 77204, U.S.A.

(Received 12 May 1997 and in revised form 18 February 1998)

Numerical results are presented for an oscillating viscous flow past a square cylinder with square and rounded corners and a diamond cylinder with square corners at Keulegan–Carpenter numbers up to 5. This unsteady flow problem is formulated by the two-dimensional Navier–Stokes equations in vorticity and stream-function form on body-fitted coordinates and solved by a finite-difference method. Second-order Adams-Bashforth and central-difference schemes are used to discretize the vorticity transport equation while a third-order upwinding scheme is incorporated to represent the nonlinear convective terms. Since the vorticity distribution has a mathematical singularity at a sharp corner and since the force coefficients are found in experiments to be sensitive to the corner radius of rectangular cylinders, a grid-generation technique is applied to provide an efficient mesh system for this complex flow. Local grid concentration near the sharp corners, instead of any artificial treatment of the sharp corners being introduced, is used in order to obtain high numerical resolution. The elliptic partial differential equation for stream function and vorticity in the transformed plane is solved by a multigrid iteration method. For an oscillating flow past a rectangular cylinder, vortex detachment occurs at irregular high frequency modes at KC numbers larger than 3 for a square cylinder, larger than 1 for a diamond cylinder and larger than 3 for a square cylinder with rounded corners. The calculated drag and inertia coefficients are in very good agreement with the experimental data. The calculated vortex patterns are used to explain some of the force coefficient behavior.

1. INTRODUCTION

THE PREDICTION OF VISCOUS FORCES acting on slender and bluff bodies with cross-sectional shapes other than circular is of practical importance in the offshore industry as well as in many other industrial applications. Viscous flow past bluff bodies is frequently associated with the phenomenon of vortex formation and shedding which has significant influence on unsteady dynamic forces and makes the problem more complicated. The physical flow for this problem oscillates back and forth past the cylinder with the axis of the cylinder perpendicular to the direction of the flow. The parameters describing this flow are the Reynolds number, $\mathrm{Re} = U_m D/\nu$, and the Keulegan–Carpenter number, $\mathrm{KC} = U_\mathrm{m} T/D$, where U_m is the maximum oscillatory velocity, T is the period of oscillation, D is the width of the cylinder perpendicular to the flow, and ν is the kinematic viscosity of the fluid. An alternate to either of these is the frequency (or Stokes) parameter defined as $\beta = \mathrm{Re}/\mathrm{KC} = D^2/\nu\mathrm{T}$. When the fluid oscillation is sinusoidal, as it is in this study, KC can be expressed as $2\pi a/D$, where a is the amplitude of fluid oscillation. For small values of KC ($\mathrm{KC} \leq 5$ at $\beta = 213$), the wake that is developed remains more or less symmetrical and

*Presently with Mauer Engineering, Houston, TX, U.S.A.

0889–9746/99/020225 + 25 $30.00

simply moves back and forth, being driven by the freestream flow as it oscillates. Due to induced velocity effects, the wake will develop asymmetries at lesser times as the value of KC increases. For larger values of KC ($KC \geq 10$), the induced velocity effects drive the wake to become oblique, it moves off to one side, has a shape similar to a Karman vortex street as in a steady approach flow, and moves back and forth as the freestream flow oscillates. For much larger values of KC, the wake again is formed only in the direction of flow; there are no oblique vortex patterns present. However, at these large values of KC, the wake is asymmetric and will be similar in appearance to the Karman vortex street behind a circular cylinder.

There are obvious implications for the force acting on the cylinder due to these various wake behaviors. The discussion in this study will focus on the low KC value case, where relatively small transverse forces are present because the wake remains (at least approximately) symmetric. Anything similar to a Karman vortex street, such as might be found at large values of KC, is not present for the parameter values considered herein. Viscous flow past a rectangular cylinder involves mathematical and physical difficulties at the sharp corners. It is well known that the vorticity distribution has a mathematical singularity on a sharp corner because of the no-slip boundary condition imposed at the location of a geometrical discontinuity. Physically, a sharp corner is a well-defined flow-separation point; the corner sharpness, r/D, of the rectangular cylinder (where r is the corner radius and D is the cylinder dimension normal to the onset-flow direction) plays an important role in determining the flow separation and reattachment, the frequency of vortex shedding, and the force coefficients.

Moffatt (1963) obtained similarity solutions for the viscous flow adjacent to a sharp corner with the assumption that the flow is Stokesian and the solution consists of the vorticity and pressure both tending to infinity at the corner. In spite of the nonexistence of the mathematical singularity in a finite-difference approximation, very large velocity, vorticity and pressure gradients appear in the immediate vicinity of a sharp corner. Many treatments have been used in previous numerical calculations to deal with the difficulties of the sharp corners for the viscous flow past rectangular cylinders.

Roache (1982) listed seven different methods of handling the vorticity boundary condition at a sharp corner in rectangular coordinates. All of the seven alternatives were attempted to compromise the difficulties in which the wall vorticity had two values at the grid point located exactly at the sharp corner. In fact, all of the seven approaches introduced artificial assumptions without any theoretical and experimental validation. It was noted that the relative quality of each of the seven methods is debatable. Roache suggested that good accuracy near the sharp convex corner would be achieved by a local analytical solution in polar coordinates centered on the corner. This approach was carried out by Fletcher & Srinivas (1983) in which a surface layer was introduced to isolate a sharp corner from the computational domain, across which the computational solution was matched to the theoretical solution for the corner flow obtained by Moffatt (1963). Moffatt's expansion method deals effectively with the situation at the corner for low Reynolds number flow. However, for high Reynolds number corner flow, which is characterized by local acceleration and separation, the Stokes flow assumption is unlikely to be satisfied.

Davis & Moore (1982) developed a numerical solution for the steady approach flow with an unsteady wake past rectangular cylinders, and they met with difficulties in determining the undefined velocities at the sharp corners of a rectangular cylinder on a staggered grid. Two assumptions were introduced to evaluate the convective flux across the control volume on both sides of the corner. The procedures described at the four corners were not the only possible ones, which may have been the reason for the Davis & Moore Strouhal number to deviate further from the experimental value with increased refinement of the mesh.

Tamura *et al.* (1990) dealt with the difficulties of a sharp corner by rounding the corner with a very small radius to try to reduce the numerical error caused by the nonsmoothness of the matrices of the transformation derivatives. However, the discontinuity of the transformation derivatives can never be essentially removed by rounding the sharp corner, until the corner radius becomes large enough so that the cross-section of the cylinder is no longer a square. Otherwise, the nonsmoothness of the matrices of the transformation derivatives always exists, which actually is a geometric characteristic of square corners.

Smith & Stansby (1991) employed the Karman–Trefftz formation and the Theodorsen–Garrick transformation to map a sharp-edged square onto a unit circle. An artificial cut-off was introduced to truncate the singular mapping derivative at each of the sharp corners. However, it was shown by Scolan & Faltinsen (1994) that the cut-off had a significant influence on the vortex motions and the drag coefficient due to skin friction. Instead of truncating the mapping derivative arbitrarily, they eliminated the singularity by replacing the Jacobian of the transformation by that for similar configurations without sharp edges. Because the singularity of the mapping derivative is actually the geometric property of the sharp-edged square, the substitutions may also change the local flow characteristics of the square cylinder with sharp corners.

It is clear that any treatment of a sharp corner may, more or less, distort not only the geometric properties but also the flow characteristics of the rectangular cylinder. It is concluded that the best way to deal with the difficulty of a sharp corner is no special treatment of the types previously attempted. In the present study, in order to simulate viscous flow past a rectangular cylinder with high accuracy, it is convenient to use body-fitted coordinates through coordinate transformations in the governing equations and boundary conditions. Owing to the one-to-one coordinate transformations (unique, single-valued), there is no difficulty encountered regarding two values of the wall vorticity at each of the four sharp corners. Even though the transformation derivatives are strongly discontinuous at the four sharp corners, which leads to a singular-like vorticity distribution near the corners, no treatment will be imposed on the sharp corners so that no artificial error is introduced. Because the very large gradients of velocity and vorticity occur near the sharp corners, a high quality mesh system with grid concentration in the neighborhood of the corners is provided by a grid generation technique to obtain high numerical resolution. Numerical convergence tests, to be presented, will prove this approach is very successful.

With the aid of powerful computational facilities and advanced numerical techniques, including grid generation and the multigrid method, the present study will provide a general and robust approach to investigate viscous flow past bluff bodies, which is concentrated on rectangular cylinders with three basic cross-sectional shapes: a square, a diamond, and a square with rounded corners. This numerical study will be more concerned with a sinusoidally oscillating viscous flow. The drag and inertia coefficients calculated from the Morison equation will be compared with the previous numerical results and the experimental data obtained by Bearman *et al.* (1984).

2. MATHEMATICAL FORMULATION

The viscous oscillatory flow of an incompressible fluid past a bluff cylinder is considered. The governing equations of the 2-D unsteady flow problem are the Navier-Stokes equations in the vorticity (ω) and stream-function (Ψ) form, which can be expressed nondimensionally in Cartesian coordinates as

$$\frac{1}{\mathrm{KC}}\omega_t + \Psi_y\omega_x - \Psi_x\omega_y = \frac{1}{\mathrm{Re}}(\omega_{xx} + \omega_{yy}), \tag{1}$$

$$\Psi_{xx} + \Psi_{yy} = -\omega, \tag{2}$$

where the subscript x indicates the partial derivative with respect to x, ω is the component of vorticity in the x direction nondimensionalized with respect to U/D, the stream function Ψ with respect to UD, t with respect to D/U, and x and y with respect to D. The term U is the maximum magnitude of the onset-flow velocity U.

The boundary conditions are

$$\Psi = \frac{\partial \Psi}{\partial n} = 0, \quad \omega = \omega_b \quad \text{on the cylinder,} \tag{3}$$

$$\Psi = \Psi_p \sin 2\pi t, \quad \omega = 0 \quad \text{far from the cylinder,} \tag{4}$$

where n is the normal to the surface of the cylinder, ω_b is the vorticity distribution on the surface of the cylinder and is determined by imposing the no-penetration and no-slip boundary conditions on equation (2), Ψ_p is the solution of the stream function for the potential flow past a rectangular cylinder and is obtained through the Schwartz–Christoffel transformation.

For a bluff body in a doubly connected region, a one-to-one transformation from the physical plane (x, y) to a generalized curvilinear coordinate plane (ξ, η) is introduced to generate a simply connected rectangular computational domain, which is defined by

$$x = x(\xi, \eta), \quad y = y(\xi, \eta). \tag{5}$$

Under the coordinate transformation, equations (1) and (2) can be mapped into the corresponding equations containing partial derivatives with respect to ξ and η as follows:

$$\frac{1}{\mathrm{KC}}\,\omega_t + \frac{1}{J}(\Psi_\eta \omega_\xi - \Psi_\xi \omega_\eta) = \frac{1}{\mathrm{Re}}\,\bar{\Delta}\omega, \tag{6}$$

$$\bar{\Delta}\Psi = -\omega, \tag{7}$$

where the operator $\bar{\Delta}$ is defined by

$$\bar{\Delta} = \frac{\alpha A_{\xi\xi} - 2\beta A_{\xi\eta} + \gamma A_{\eta\eta}}{J^2} + \frac{(\alpha x_{\xi\xi} - 2\beta x_{\xi\eta} + \gamma x_{\eta\eta})(y_\xi A_\eta - y_\eta A_\xi) + (\alpha y_{\xi\xi} - 2\beta y_{\xi\eta} + \gamma y_{\eta\eta})(x_\eta A_\xi - x_\xi A_\eta)}{J^3} \tag{8}$$

with A as either Ψ or ω. The transformation parameters are

$$J = x_\xi y_\eta - x_\eta y_\xi, \quad \alpha = x_\eta^2 + y_\eta^2, \quad \beta = x_\xi x_\eta + y_\eta y_\xi, \quad \gamma = x_\xi^2 + y_\xi^2. \tag{9}$$

The boundary conditions under the transformation become

$$\psi = \frac{\gamma^{1/2}}{J}\psi_\eta = 0 \quad \text{and} \quad \omega = \frac{\gamma}{J^2}\,\psi_{\eta\eta} \quad \text{on } \eta = 0, \tag{10}$$

$$\psi = \psi_p \sin 2\pi t \quad \text{and} \quad \omega = 0 \quad \text{on} \quad \eta = 1. \tag{11}$$

The periodic boundary conditions are imposed on $\xi = 0$ and $\xi = 1$. Since the flow starts from rest, the initial conditions throughout the field are

$$\psi = 0, \qquad \omega = 0. \tag{12}$$

The pressure coefficient is derived from the integration of the momentum equation along the surface of the cylinder, which is given in the transformed plane by

$$C_p = \frac{1}{\mathrm{Re}} \int_0^{\xi} \frac{1}{J}(\beta\omega_{\xi'} - \gamma\omega_{\eta})\mathrm{d}\,\xi'. \tag{13}$$

The in-line force and lift coefficients in the transformed plane are denoted C_F and C_L, respectively, and are found by integrating the pressure and shear stress distribution around the cylinder,

$$C_F = 2\int_0^1 \left(y_\xi C_p - \frac{1}{\mathrm{Re}}\, x_\xi \omega\right)\mathrm{d}\xi, \tag{14}$$

$$C_L = -2\int_0^1 \left(x_\xi C_p + \frac{1}{\mathrm{Re}}\, y_\xi \omega\right)\mathrm{d}\xi, \tag{15}$$

The standard method of representing the dimensionless in-line force coefficient C_F on a cylinder of any cross-section in a sinusoidally oscillating flow is based on the Morison equation [see Sarpkaya & Isaacson (1981)],

$$C_F = C_D \sin\theta\,|\sin\theta| + C_M \frac{\pi^2}{\mathrm{KC}}\cos\theta. \tag{16}$$

The values of the drag coefficient C_D and the inertia coefficient C_M can be obtained from

$$C_D = \frac{3}{8}\int_0^{2\pi} C_F \sin\theta\,\mathrm{d}\theta. \tag{17}$$

$$C_M = \frac{\mathrm{KC}}{\pi^3}\int_0^{2\pi} C_F \cos\theta\,\mathrm{d}\theta. \tag{18}$$

3. NUMERICAL IMPLEMENTATION

In the present computation, grid systems are produced by GENIE2D, a grid-generation package created in the NSF Engineering Research Center at Mississippi State University, using an algebraic grid generation method. The near corner grid system for a square cylinder (one-quarter of the cylinder side) is shown in Figure 1. The grid for flow past a diamond cylinder is obtained by considering the flow to be from a 45° angle of attack, as is also shown in Figure 1. Apart from the grid concentration very close to the body surface in the radial direction, grid concentration is also arranged locally near the four sharp corners of the square and diamond cylinders, to increase the numerical resolution near the corners with very large gradients of velocity and vorticity. All of the transformation derivatives and parameters in equation (9) are approximated by second-order central-difference expressions.

The vorticity transport equation is explicitly discretized in time by using the second-order Adams–Bashforth scheme. All of the spatial discretizations are second-order central-difference schemes, except the nonlinear convective terms in equation (6). The third-order upwinding scheme proposed by Leonard (1979) is applied to approximate these convective terms. Due to the existence of mixed derivatives and variable coefficients in equation (7), it is impractical to solve it by using the spectral method incorporating the FFT algorithm with high efficiency. The multigrid iteration method is the most efficient approach to solve equation (7).

A multigrid solver was developed by Sanders (1992) to solve the two-dimensional Helmholtz equation,

$$\nabla \cdot (A(x)\nabla u) - \alpha u + f(x) = 0. \tag{19}$$

where $A(x), f(x)$ and $u(x, y)$ are arbitrary functions and α is a constant. In the present study, the multigrid solver has been developed to solve a 2-D elliptic partial differential equation with mixed derivatives, first-order derivatives and variable coefficients,

$$a_1 u_{xx} + a_2 u_{xy} + a_3 u_{yy} + a_4 u_x + a_5 u_y + a_6 u + f = 0, \tag{20}$$

where a_1, a_2, a_3, a_4, a_5, a_6, f, and u are arbitrary functions of x and y. For viscous flow past rectangular cylinders, the grid system is characterized by discontinuous transformation derivatives near the four sharp corners, which correspondingly lead to the strongly discontinuous coefficients in equation (9). This multigrid solver possesses the capability of solving elliptic partial differential equations with discontinuous coefficients. It has been shown in various numerical tests that the multigrid solver has a solid dependability of accurately solving elliptic partial differential equations with higher efficiency than the SOR iteration method with Chebyshev acceleration (Sanders 1992). The multigrid solver has been optimized herein to run at more than 350 megaflops on the Cray C90 at the Pittsburgh Supercomputer Center.

The vorticity boundary condition in equation (10) on the body surface can be expressed in terms of the stream function in the interior mesh points with second-order accuracy, using the Taylor series expansion with the implication of the no-slip condition,

$$\omega_{i,1} = \frac{\gamma_{i,1}}{(J_{i,1}\Delta\eta)^2}(7\psi_{i,1} - 8\psi_{i,2} + \psi_{i,3})/2, \tag{21}$$

where $\Delta\eta$ is the grid spacing in the η direction in the transformed plane.

4. VALIDATION OF THE NUMERICAL METHODS

Convergence validation of numerical methods has been a difficult and controversial issue for unsteady viscous flow past bluff cylinders, especially with cylinders with sharp corners. Generally speaking, convergence in space is more crucial than that in time, due to the existence of large spatial gradients. The lack of spatial convergence also leads to a failure of convergence in time which is distinct from an instability. The vorticity distribution on the body surface is usually the best choice to demonstrate the spatial convergence of the numerical solutions in the vorticity/stream-function formulation. However, for viscous flow past a rectangular cylinder, the wall-vorticity distribution has a mathematical singularity on the sharp corners of the cylinder, which then never has a converged numerical solution. In the previous numerical studies of viscous flow past rectangular cylinders, several approaches have been used to show convergence in space. Davis & Moore (1982) used the Strouhal number and the average in-line force coefficients for a square cylinder as the characteristic quantities to exhibit the variations with mesh sizes and the comparisons to experimental data. Smith & Stansby (1991) showed the influence of the artificial cut-off of the mapping derivative on the drag coefficients for oscillating flow past a diamond cylinder. Tamura *et al.* (1990) presented the effects of grid spacing on the computed in-line force coefficients and the flow patterns of a circular cylinder. However, the Strouhal number and the force coefficients are not the direct solutions of the numerical methods and are calculated through time averaging. Therefore, it is doubtful that these quantities can

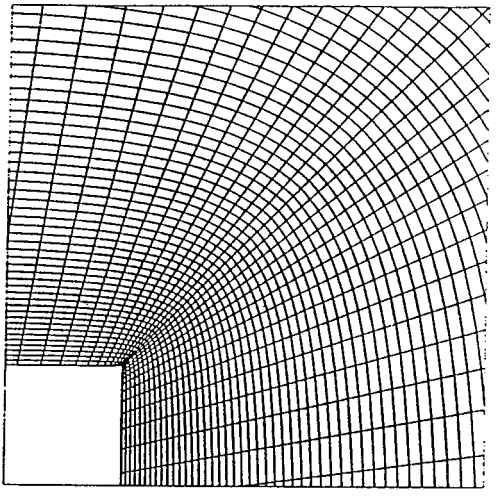

(a) around a sharp corner of a square cylinder

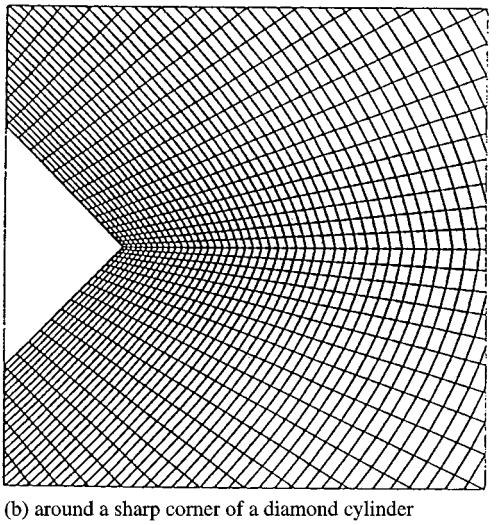

(b) around a sharp corner of a diamond cylinder

Figure 1. Local grid concentration.

provide clear measures of convergence in space. As to the flow pattern, it is a space- and time-dependent quantity and may not be used directly to trace the convergence trends, especially for unsteady flow problems.

In the present study, beside the instantaneous wall-vorticity distribution, the instantaneous pressure coefficient on the surface of rectangular cylinders is utilized to demonstrate the spatial convergence of the numerical methods. The instantaneous pressure coefficient has finite magnitude and is calculated from direct integration of the wall-vorticity derivatives on the body surface. Convergence tests have been conducted for a sinusoidally oscillating viscous flow past a square cylinder at $\beta = 432$ and $\mathrm{KC} = 1$. Two types of grid distributions in the circumferential direction are tested; one is a uniform distribution and another is a hyperbolic tangential distribution with local grid concentration close to each of the four sharp corners shown in Figure 1. The minimum mesh sizes in the η direction in the

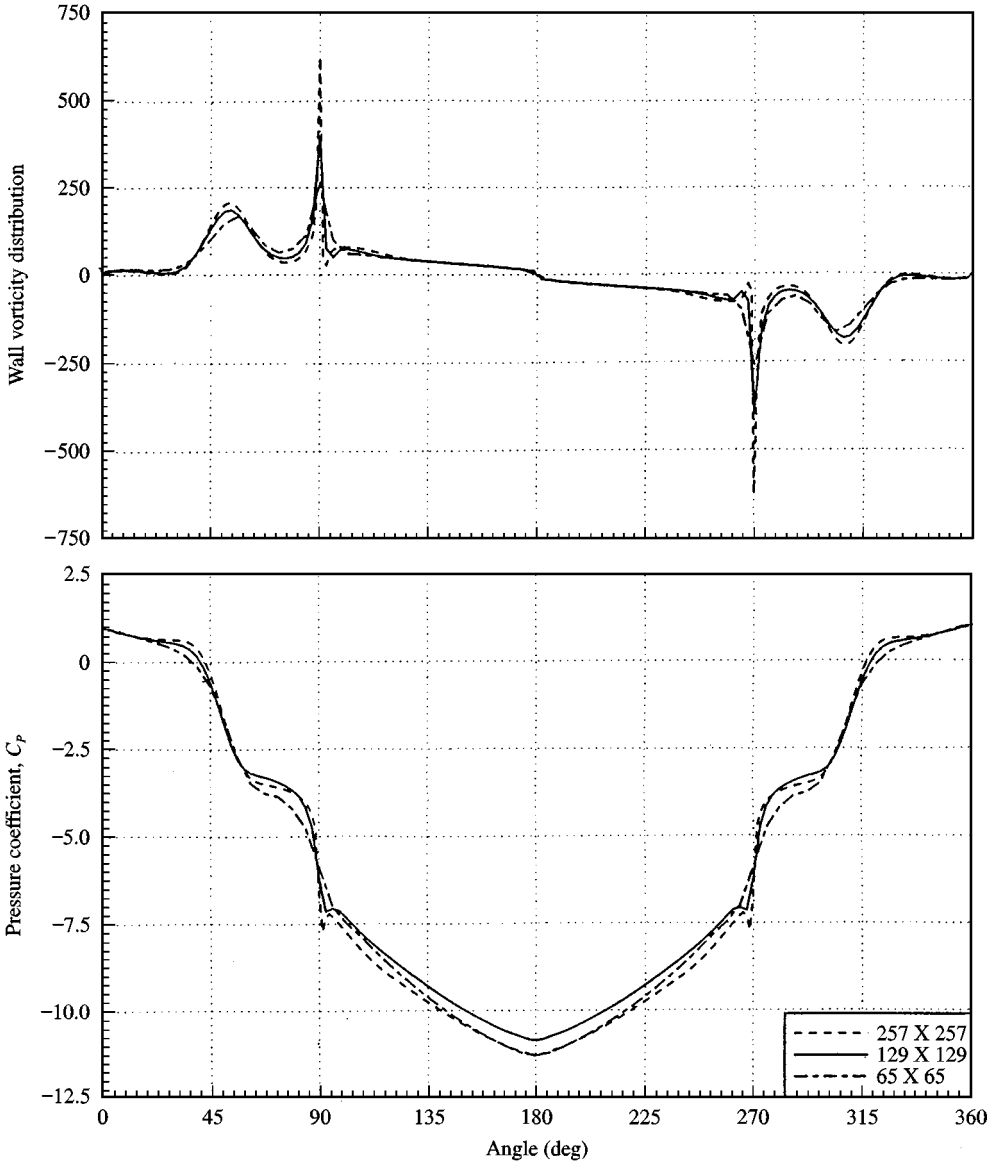

Figure 2. Influence of mesh size on the wall-vorticity distributions and pressure coefficients for oscillating flow past a diamond cylinder without local grid concentration at $\beta = 432$, KC = 1, and $t = 2$.

physical plane are given by 0·02, 0·01 and 0·005 on 65×65, 129×129 and 257×257 grids, respectively. The minimum mesh sizes in the circumferential direction in the physical plane are 0·005, 0·0025 and 0·00125 for the square cylinder in the cases with local grid concentration near the four sharp corners, and 0.01, 0.005 and 0.0025 for the diamond cylinder on the three different grids, respectively. The maximum distance between the center of the cylinders and the outer boundary is specified as $10D$. The width D of the square and the diamond cylinders normal to the flow direction is specified as unity. The time step Δt is 0·0005, 0·00025 and 0·000125 for the square cylinder and the diamond cylinder on the three different grids, respectively. The calculations were done on our Silicon Graphics Indigo

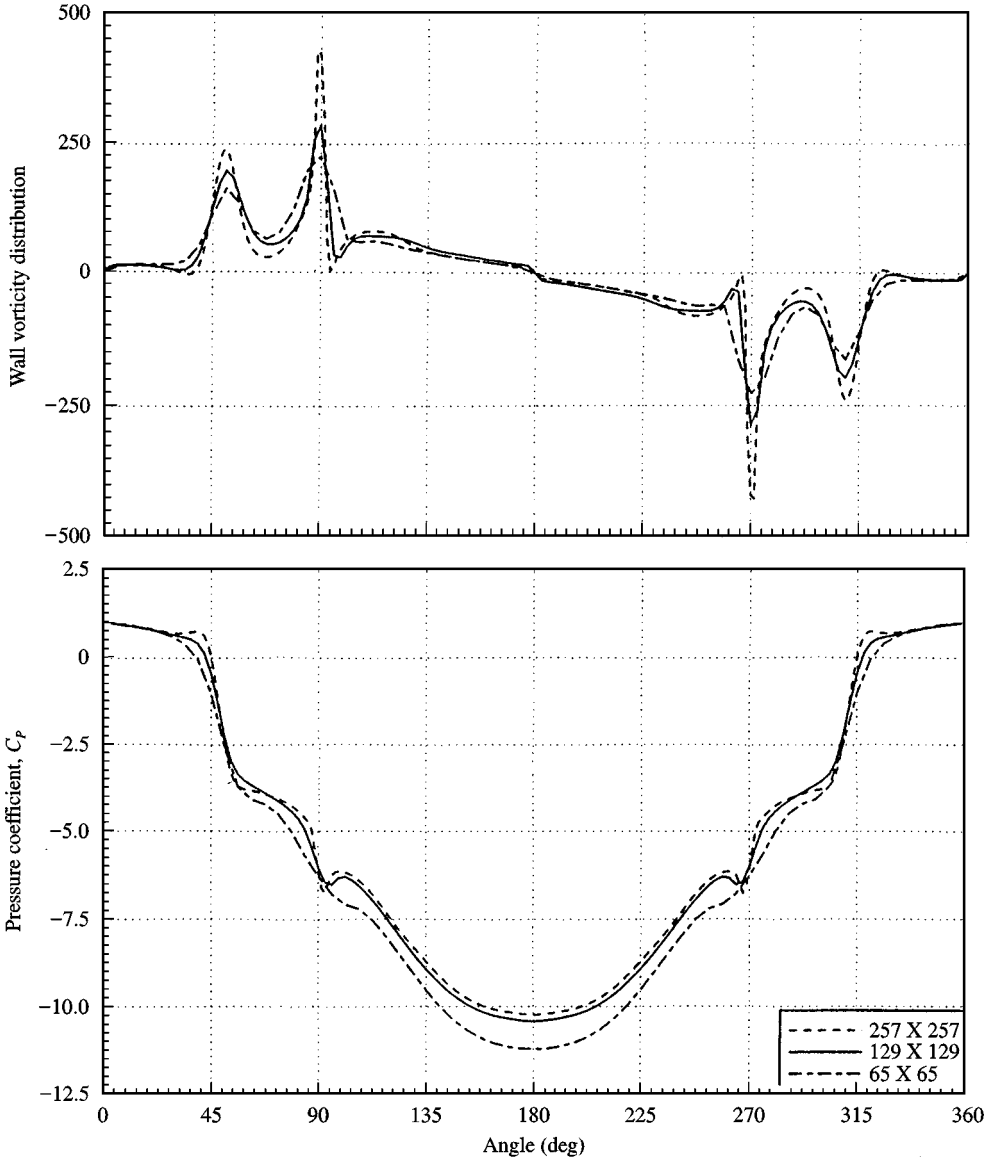

Figure 3. Influence of mesh size on the wall-vorticity distributions and pressure coefficients for oscillating flow past a diamond cylinder with local grid concentration at $\beta = 432$, KC = 1, and $t = 2$.

R4000 Work Station and on the Cray C90 at the Pittsburgh Supercomputing Center. It took approximately 2 h to calculate one cycle on the SGI Work Station and about 10 min per cycle on the Cray C90.

Figure 2 shows the wall-vorticity distributions and pressure coefficients at time $t = 2$ for the diamond cylinder on the three different grids with uniform grid distribution (no grid concentration) in the circumferential direction. The wall-vorticity distributions behave in a singular fashion on the four sharp corners of the cylinder, which makes the pressure coefficients have a big jump at the corners. It is observed from Figure 2 that the peaks in the wall-vorticity significantly increase with decreasing mesh sizes. It is also noted that the

TABLE 1

Comparisons of the drag and inertia coefficients on 129×129 grids with and without grid refinement for oscillating flow past square and diamond cylinders

		C_D without gird refinement	C_M without grid refinement	C_D with grid refinement	C_M with grid refinement	Bearman *et al.* experimental C_D	Bearman *et al.* experimental C_M
Square	$\beta = 213$ KC = 1	13·31	3·36	3·07	2·99	3·19*	2·78
Diamond	$\beta = 432$ KC = 1	8·28	1·69	4·71	1·63	4·6	1·69

*Interpolated.

pressure coefficient did not converge as the number of grid points increased for this case of a uniform grid distribution.

The case in Figure 3 is the same as in Figure 2, but with local grid concentration near the sharp corners in the circumferential direction. Even though the wall-vorticity distributions in the immediate vicinity of the four sharp corners still go up drastically due to its singular property, the other part of the distributions tend to be convergent as the mesh sizes are refined. As for the pressure coefficients, distinct convergent trends are found in Figure 3, even around the four sharp corners. The pressure coefficients become smooth around the sharp corners of the cylinder with local grid concentration, instead of the discontinuous distributions on the sharp corners without local grid refinement.

Comparison of Figures 2 and 3 shows that it is the local grid concentration near the sharp corners that makes convergence realizable. Table 1 shows that the calculated drag and inertia coefficients on the 129×129 grids with local grid concentration are in very good agreement with the experimental values obtained by Bearman *et al.* (1984), while those on the 129×129 grid without grid concentration deviate significantly from the experimental data. From the convergence test conducted, it is concluded that the numerical results have converged satisfactorily for the square and diamond cylinders on the 129×129 grids with local grid concentration.

5. RESULTS AND DISCUSSION

5.1. SQUARE CYLINDER

A sinusoidally oscillating flow past a square cylinder was computed for 10 flow cycles on a 129×129 grid with local grid concentration at $\beta = 213$ and KC number ranging from 1 to 5. The minimum mesh size in the η direction in the physical plane is 0.01 while the hyperbolic tangentially distributed (local) grid concentration near each of the four sharp corners is imposed in the circumferential (ξ) direction with the minimum mesh size equal to 0·0025 in the physical plane. The maximum dimensionless distance r_∞ between the center of the cylinder and outer boundary is 10. The time step Δt is 0·00025 at KC = 1, 2 and 3, but is 0·0002 at KC = 4 and 5. In each case to be discussed, the starting flow always occurred from left to right.

Figures 4–6 show the vorticity plots for KC numbers of 1, 3, and 5 at several dimensionless times through a multicycle oscillation. The KC number for sinusoidal oscillations is $2\pi a/D$, where a is the amplitude of oscillation and D is the square cylinder width. In each

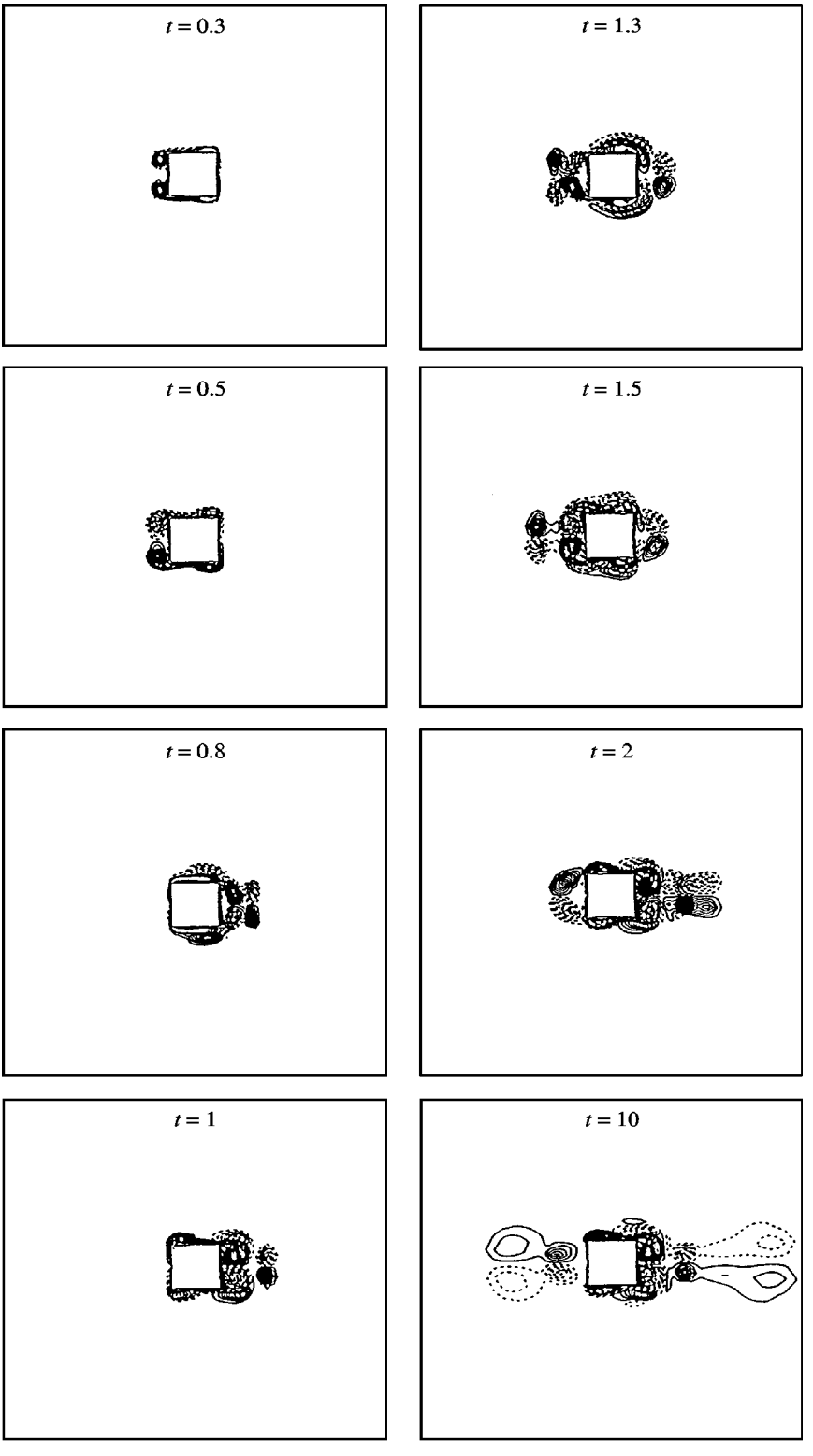

Figure 4. Vorticity distribution on a square cylinder for KC = 1 at different dimensionless times, $\beta = 213$.

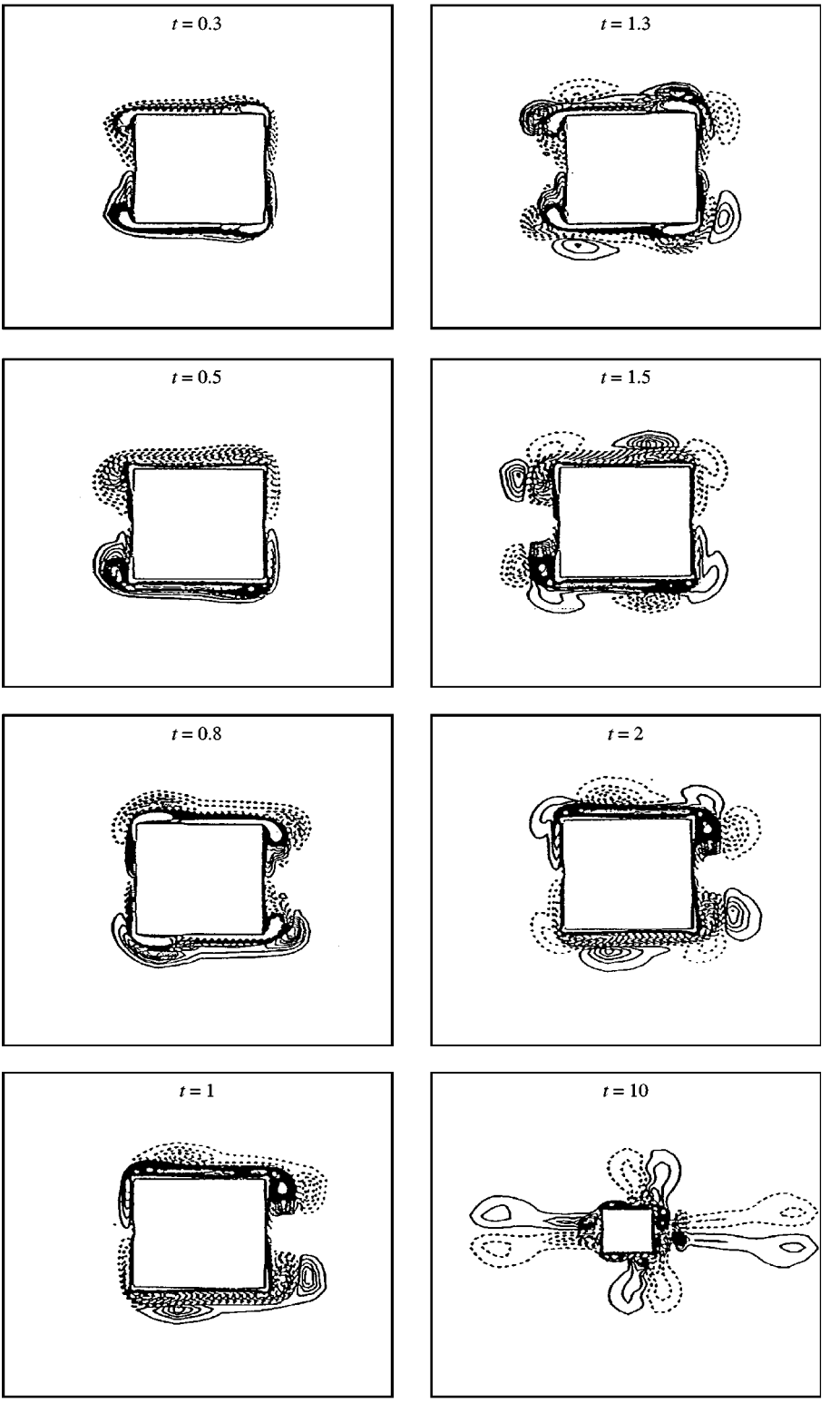

Figure 5. Vorticity distribution on a square cylinder for KC = 3 at different dimensionless times, $\beta = 213$.

case, the solid lines represent positive vorticity while the dashed lines represent negative vorticity. Also, the grid is the 129×129 mesh with grid concentration in each case.

Figure 4 shows the vorticity behavior through two complete cycles of oscillation and at the end of the 10th cycle for KC = 1 and $\beta = 213$. At this low value of KC, the a/D value is $1/(2\pi)$, which is quite small and the flow would be expected to remain symmetric with the wake vortices close to the cylinder, i.e., no vortices are shed during these two oscillatory cycles. (This statement will be verified later when Figure 7 is discussed.) During the first half cycle ($t \leq 0{\cdot}5$), the layers of positive and negative vorticity on each side of the cylinder are evident. As the flow reverses and the return flow part of the first cycle begins, the original vorticity layers are pushed outward from the sides of the cylinder as new layers of oppositely signed vorticity are formed. Note that these newly formed vorticity layers wrap around the corners of the cylinder. At the beginning of the second cycle ($t = 1{\cdot}1$), the outside vorticity layer on each side splits to become two distinct regions of like-sign vorticity. As the flow continues through this time range ($1{\cdot}0 \leq t \leq 1{\cdot}5$), the vortical structures become more complicated, but remain symmetric. A new layer of vorticity forms on either side of the square cylinder with the layer remaining from the previous half cycle located just outside this newly formed layer. The vorticity from the original half-cycle has now formed distinct unattached regions of recirculating flow, external to the two attached layers. This same process continues in the fourth half-cycle with the vorticity from the first two half-cycles having formed distinct recirculation regions of opposite-sign vorticity. The vorticity from the last two half-cycles still exists over the sides of the cylinders. The remaining part of Figure 4 shows the vorticity patterns at the end of the 10th cycle. The vortex structures are more complicated and more extensive, but they remain symmetric as expected.

Figure 5 shows the behavior of the vorticity for a 10-cycle oscillation for KC = 3 and $\beta = 231$. In this case, the oscillation amplitude is three times as much as for the KC = 1 situation. Even so, the flow does remain symmetric over at least 10 cycles (as will be noted in Figure 8). The first half-cycle here is similar to the previous case (KC = 1). However, the splitting of the original (first half-cycle) vorticity layers in this case leads to part of them appearing as distinct and separated wake vortices in the second half-cycle. The larger velocity in the KC = 3 case (relative to KC = 1) induces the distinct vortex structures from the first half-cycle to move farther downstream, i.e., more into the wake of the second half-cycle. As the second cycle begins, the same process is repeated, except that the two vortex structures that had moved into the wake of the previous half-cycle remain there, although they do move closer to the cylinder. So, at the end of the third half-cycle, each end of the square cylinder has two distinct pairs of opposite-sign vortices present. As the flow reverses again, new distinct vortex structures have formed and move into the region which was the wake of the second half-cycle. The new and previous distinct vortex structures (of like sign) merge to form one vortex of extended length. In addition to the formation of these wake vortices, the flow along the sides of the cylinder produced the dual layer of opposite-sign vorticity as in the KC = 1 case. The vortex structures at $t = 10$ show that the flow has remained symmetric through at least the first ten cycles of oscillation at KC = 3.

The last case for a square cylinder, shown in Figure 6 for KC = 5 and $\beta = 213$, becomes asymmetric rather quickly. For KC = 5, the a/D value is $5/(2\pi)$ which still seems rather small, but now vortices are both convected and induced up to six diameters downstream by the eighth cycle. By the end of the first half cycle for this case, the vortex pattern is asymmetric. The dual wake vortices at the end of the second half cycle have moved much further downstream than for the KC = 3 case. The vorticity on the sides of the cylinder

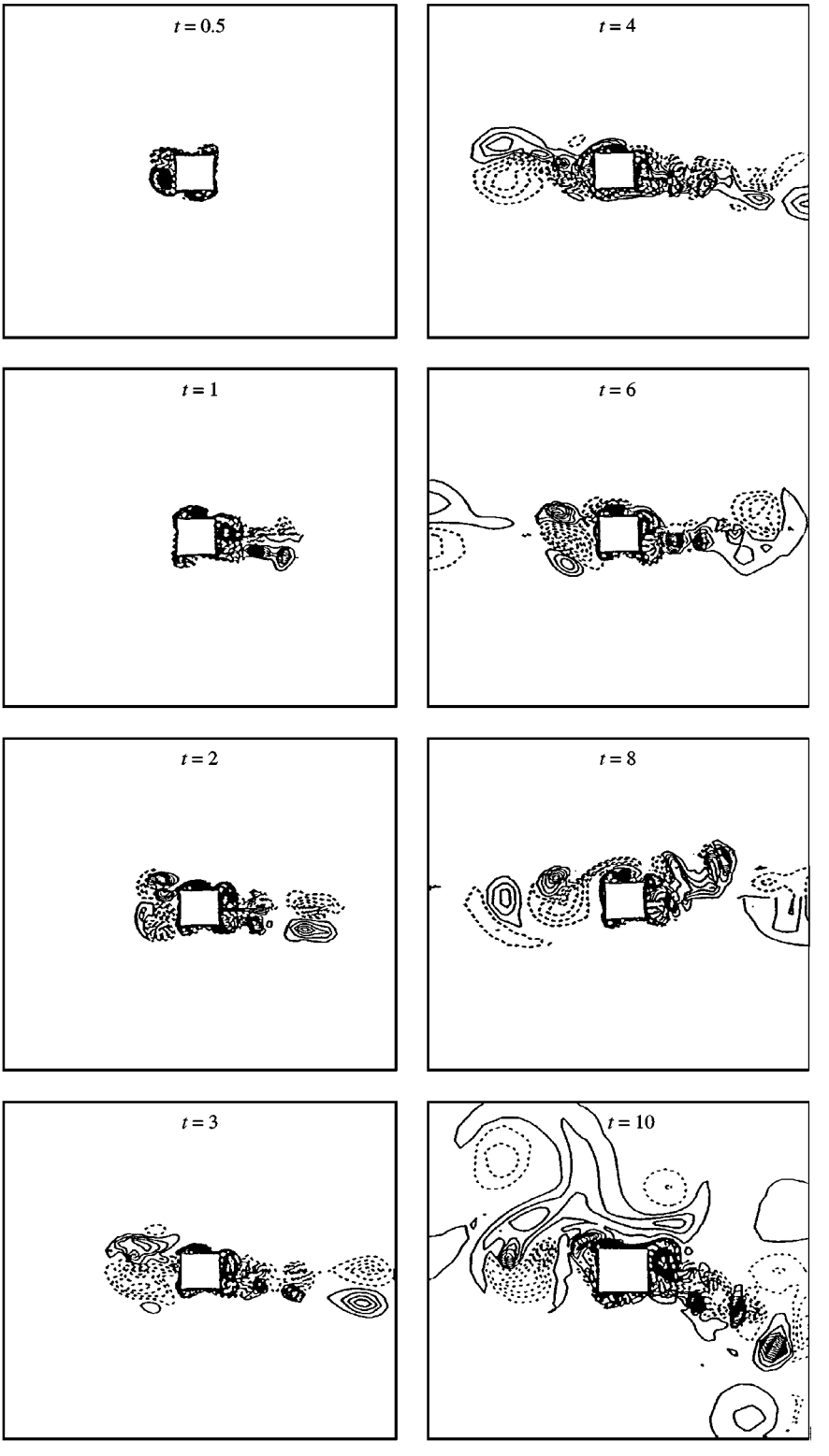

Figure 6. Vorticity distribution of a square cylinder for KC = 5 at different dimensionless times, $\beta = 213$.

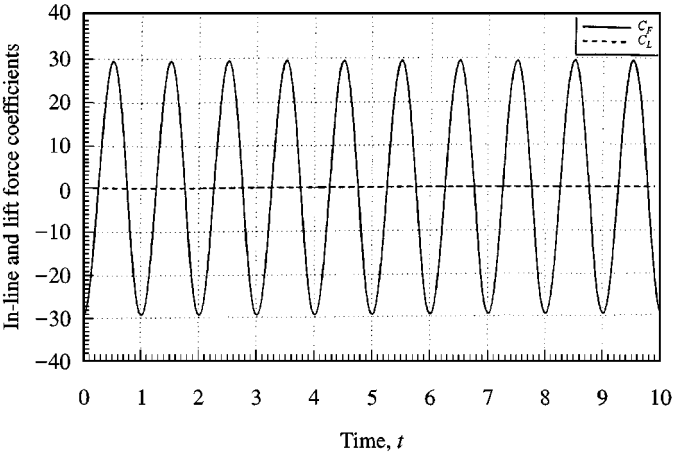

Figure 7. In-line force and lift coefficients for a square cylinder at $\beta = 213$ and KC = 1.

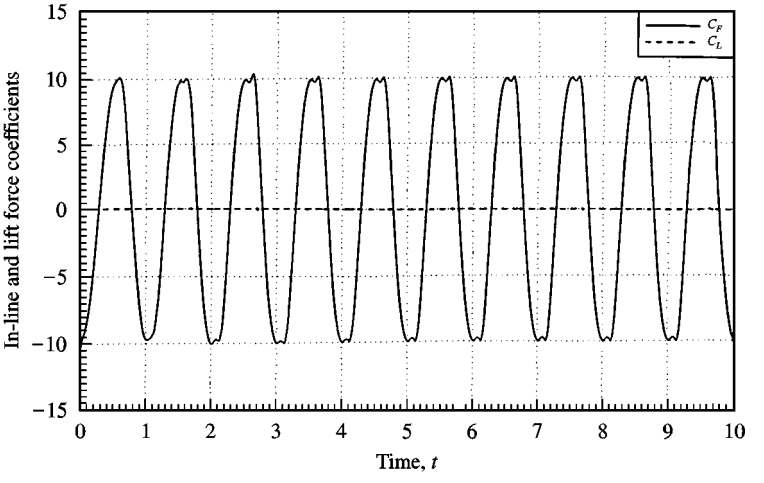

Figure 8. In-line force and lift coefficients for a square cylinder at $\beta = 213$ and KC = 3.

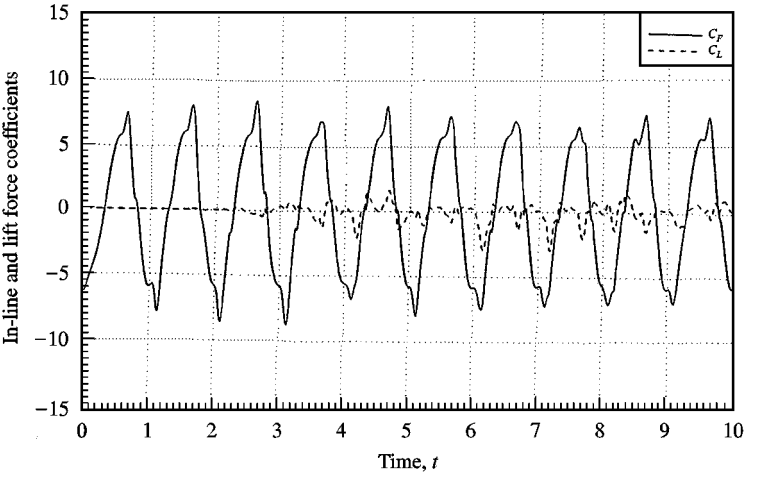

Figure 9. In-line force and lift coefficients for a square cylinder at $\beta = 231$ and KC = 5.

TABLE 2

Comparisons of the drag and inertial coefficients for oscillating flow past a square cylinder at $\beta = 213$

KC number	Present calculated C_D	Present calculated C_M	Scolan & Faltinsen calculated C_D	Scolan & Faltinsen calculated C_M	Bearman *et al.* experimental C_D	Bearman *et al.* experimental C_M
1	3·01	2·99	4·39	2·98	3·19*	2·78
2	3·21	3·07	3·61	2·99	3·15	3·06
3	3·19	3·23	3·19	3·04	2·84	2·89
4	2·40	3·21	2·76	3·07	2·42	2·96
5	2·38	3·08	2·28	3·09	2·27	3·13

*Interpolated.

follows the same dual layer behaviour as for the lower KC values. The process repeats itself as the number of cycles goes up with the asymmetry increasing. In spite of the downstream distance these wake vortices have moved, conventional vortex shedding of the alternating and periodic type has not yet occurred. The downstream-distance movement is primarily due to induced velocity effects.

Figures 7–9 present the variations of the in-line force coefficient C_F and the lift coefficient C_L at KC numbers of 1, 3, and 5. The variation of the in-line force coefficient is smooth, periodic and symmetric with respect to the axis of the onset-flow oscillation, and the lift coefficient is equal to zero at KC = 1; both are shown in Figure 7. At KC = 3 (Figure 8), a small "dent" at each peak of the curve of the in-line force coefficient has appeared, but the influence is not so strong since the in-line force coefficient remains regular, periodic, and symmetric. We attribute this dent to the effect of induced velocity as the freestream velocity comes to rest at the end of each half cycle. At KC = 5 (Figure 9), the variation of the in-line force coefficient is characterized by some fluctuations of the magnitude of each peak with irregular frequency modes and a sharp angle at each peak of the curve. This behavior is obviously characterized by the asymmetric motion of the vortex structure surrounding the cylinder.

Asymmetrical modes begin to appear at KC numbers larger than 3 and develop to contribute a nonzero value of the lift coefficient at KC = 5. The irregular high-frequency modes in the force coefficient are believed to be induced by the flow asymmetry and the interaction between the frequency of the onset-flow oscillation and the frequency of the vortex detachment. Nevertheless, the in-line force coefficients are dominated by the effects of the forced oscillation of the onset flow, even though the high frequency modes have strong effects on them. Therefore, it is reasonable to calculate the drag and inertia coefficients from Morison's equation with the computed in-line force coefficients averaged over the last five of the 10 flow cycles at KC numbers above 3, where the flow structure has become fully established and the inertial effect from starting the flow from rest has vanished.

It is shown in Table 2 that the calculated drag and inertia coefficients at KC from 1 to 5 are in very good agreement with the experimental data obtained by Bearman *et al.* (1984). These calculated values are obtained from the last five cycles of the oscillating freestream flow. The calculated drag and inertia coefficients in the present study are typically closer to the experimental data than those in the study of Scolan & Faltinsen (1994) which were obtained by using the same random-vortex method as Smith & Stansby (1991) with some correction.

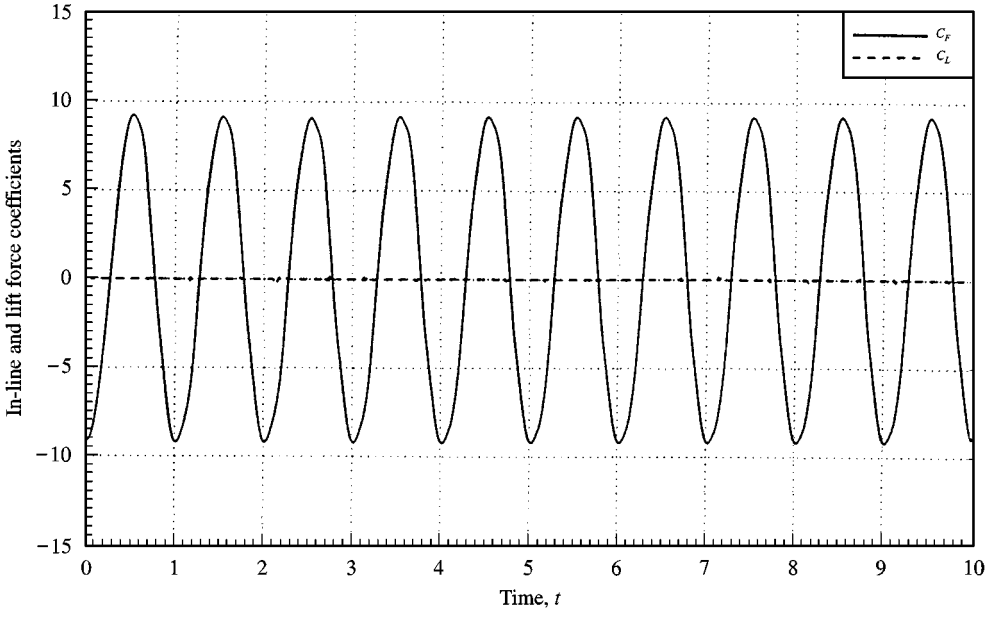

Figure 10. In-line force and lift coefficients for a square cylinder with rounded corners ($r/D = 0{\cdot}132$) at $\beta = 172$ and KC = 3.

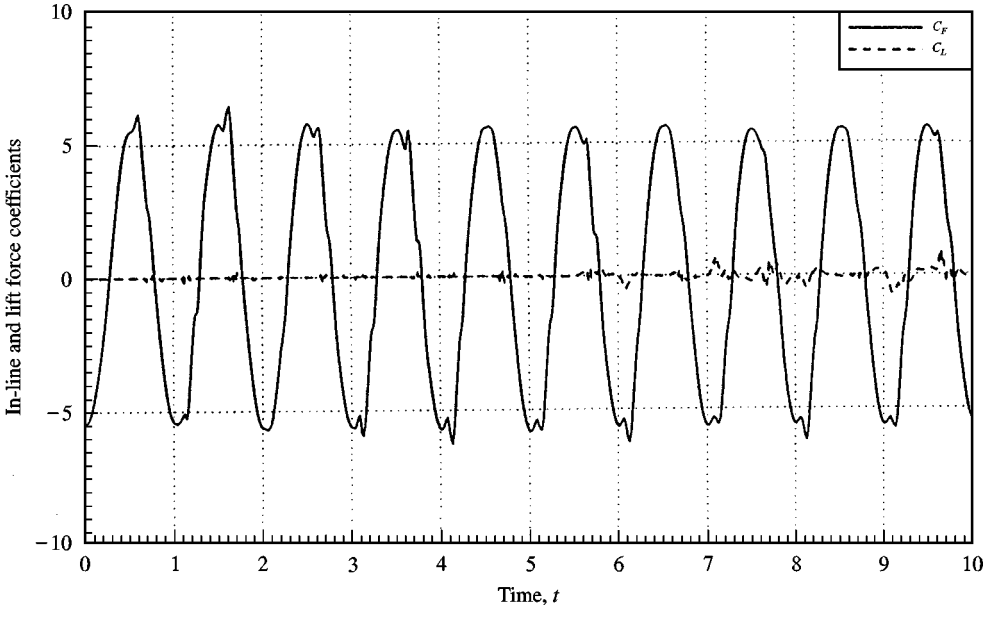

Figure 11. In-line force and lift coefficients for a square cylinder with rounded corners ($r/D = 0{\cdot}132$) at $\beta = 172$ and KC = 5.

5.2. Square Cylinder with Rounded Corners

The numerical computation of sinusoidally oscillating flow past a square cylinder with rounded corners, $r/D = 0{\cdot}132$, was performed for ten flow cycles on a 129×129 grid at

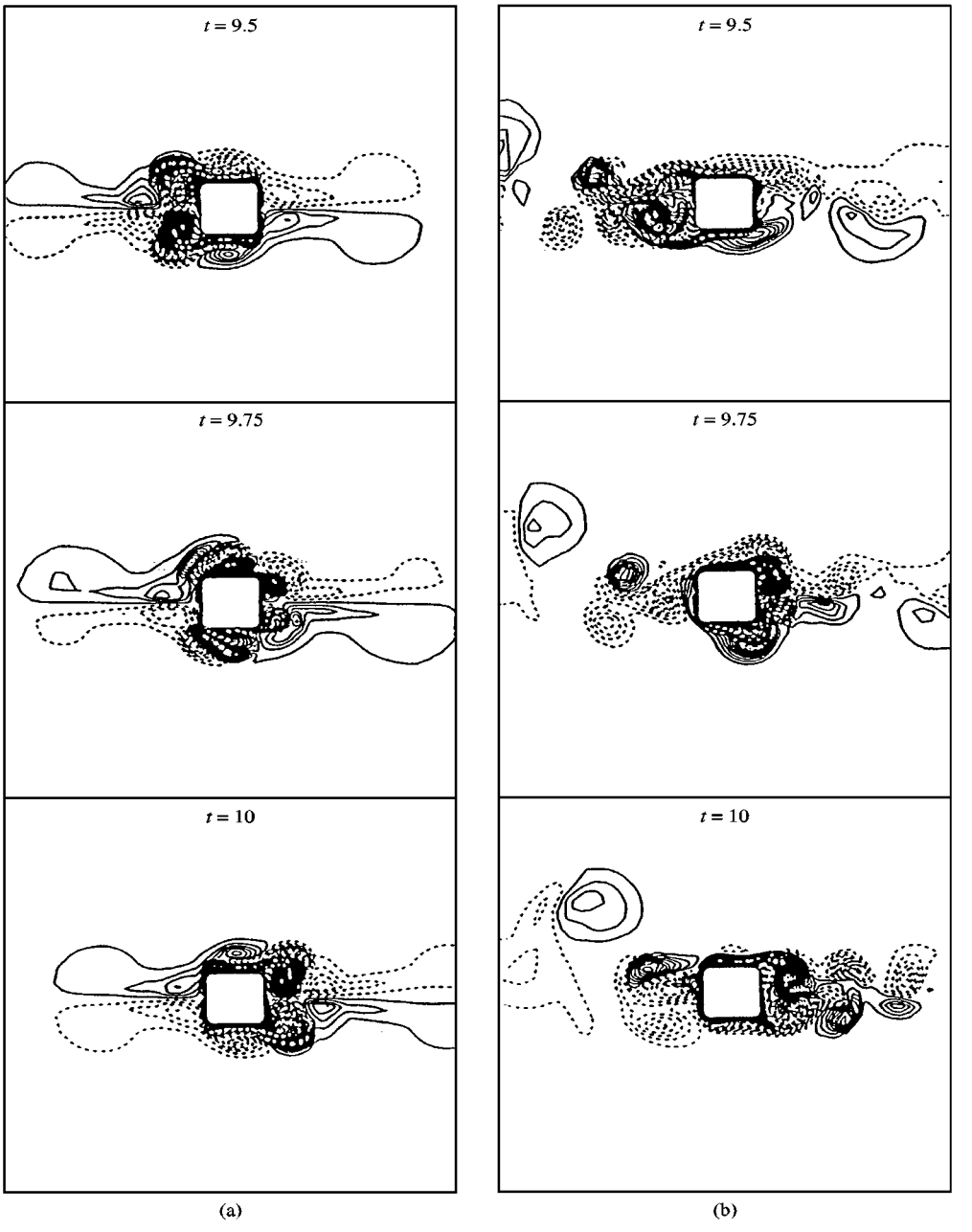

Figure 12. Near field of vorticity contours on a square cylinder with rounded corners ($r/D = 0{\cdot}132$) at $\beta = 172$ for (a) KC = 3 and (b) KC = 5, at three different dimensionless times.

$\beta = 172$ and KC numbers ranging from 1 to 5, where r is the radius of each rounded corner of the cylinder. The minimum mesh size in the η direction is 0·01 in the physical plane for $KC \leq 2$ and 0·005 at $KC > 2$, while the grid distribution in the circumferential direction is uniform due to no singularity of wall vorticity distribution involved for the square cylinder with rounded corners. The maximum dimensionless distance between the center of the cylinder and the outer boundary is 10. The time step Δt is 0·001 at KC = 2 and 0·0005 at KC > 2.

TABLE 3

Comparisons of the drag and inertial coefficients for oscillating flow past a square cylinder with rounded corners, $r/D = 0{\cdot}132$, at $\beta = 172$

KC number	Present calculated C_D	Present calculated C_M	Smith & Stansby calculated C_D	Smith & Stansby calculated C_M	Bearman *et al.* experimental C_D	Bearman *et al.* experimental C_M
2	2·6	2·84	2·38	2·75	2·18	2·86
3	2·37	2·80			2·44	2·75
4	1·98	2·79			1·93	2·82
5	1·81	2·92			1·71	2·89

Figures 10 and 11 show the variation of the in-line force and lift coefficients for KC = 3 and 5. At KC = 3, the variation of the in-line force coefficient is similar to that at KC = 1, but with a little sharper angle at the peaks of the curve and the lift coefficient has a very small disturbance, from which asymmetric modes begin to appear. At KC = 5, asymmetric modes have a significant influence on the in-line and lift force coefficients with fluctuations and irregular high frequencies. The lift coefficient shows the effects of the beginning of wake asymmetries.

There is a noticeable difference between the results for the cylinders with rounded and unrounded corners. Figure 12(a) shows the vortex patterns for the rounded-corner cylinders for KC = 3 and $\beta = 172$. The vortex structures in the case for $\beta = 213$ (square corners) in Figure 5 are distinct, while those in the $\beta = 172$ case (rounded corners) in Figure 12 are still connected to the cylinder. Even though the β values are slightly different, the difference should not account for the break in the vortex structures seen in Figure 5. The effect of square corners is far more evident in Figure 12(b) where the vorticity contours for the rounded-corner cylinder are shown for KC = 5. The results for $\beta = 213$ (square corners) show a disorganized wake structure while the case for $\beta = 172$ (rounded corners) shows a more organized structure. The square corners are evidently responsible for the disorganized structure in the $\beta = 213$ case. Thus, we feel that the difference in vortex structures is due to the effect of the rounded corners, and is not due to the slight difference in β values between the two cases.

A comparison of Figure 8 (square corners) and Figure 10 (rounded corners) reveals the absence in the rounded-corners results of the small oscillations at the maximum and minimum points on the inline force that were present in the square-corner results. The peak values for the rounded-corner results are also slightly less than the peak values for the square-corner case. The differences are attributed to the stronger vorticity generated in the square-corner example. We also note that the lift force is zero for KC = 3 through 10 cycles, indicating that the vortex structures remained symmetric. However, for KC = 5, the square-corner lift coefficient (in Figure 9) has begun to show nonzero values at a dimensionless time as early as $t = 2{\cdot}5$, indicating an asymmetric wake structure. Also, the rounded-corner lift coefficient (in Figure 11) indicates a fairly symmetric wake until a dimensionless time of about 6 with only a small deviation from zero until a time of about 9, indicating a delay in wake asymmetry which we attribute to the rounded corners.

It is shown in Table 3 that the calculated drag and inertia coefficients at $\beta = 172$ and at KC numbers from 2 to 5 are in very close agreement with the experimental data obtained by Bearman *et al.* (1984).

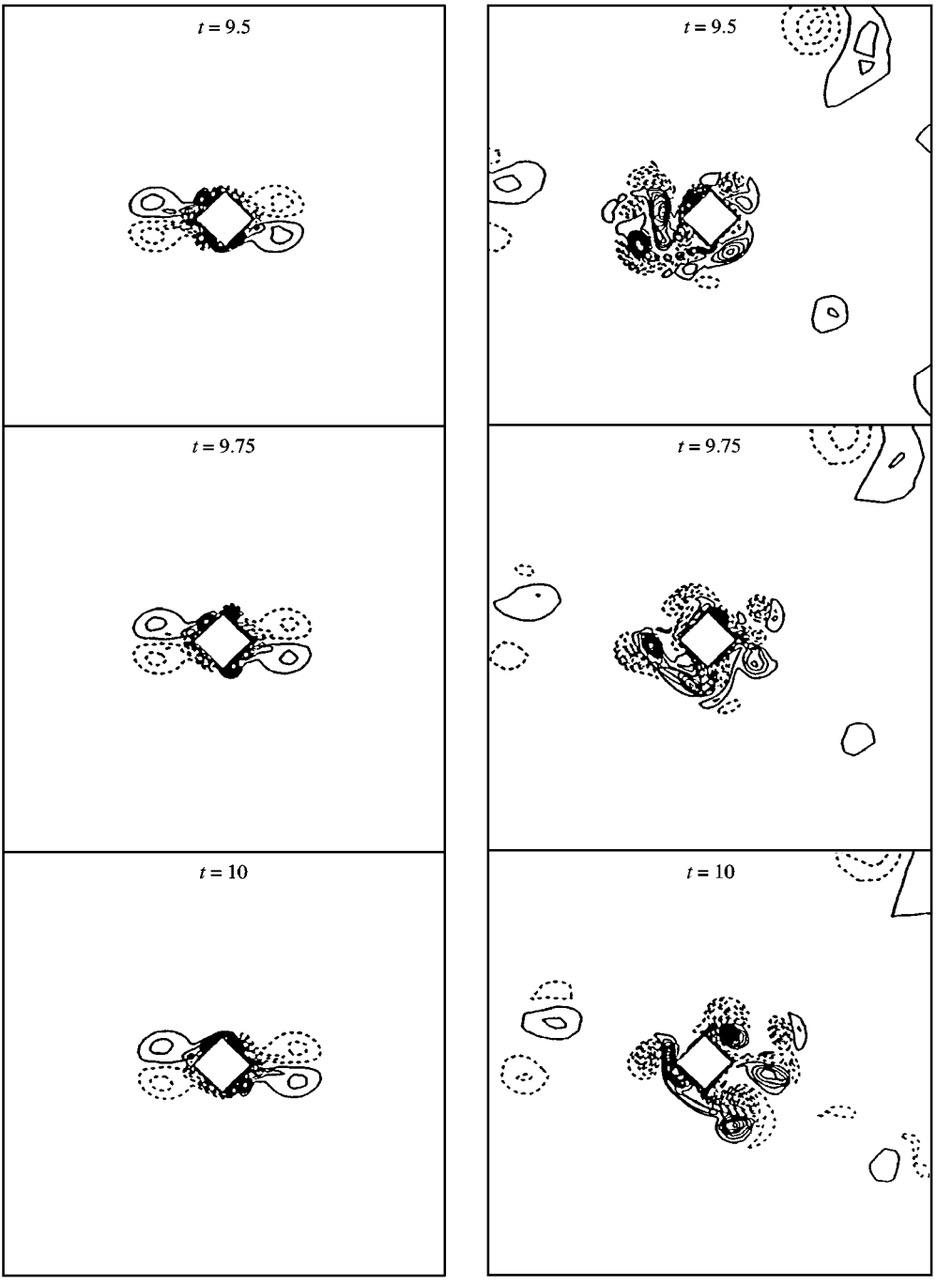

Figure 13. Near field of vorticity contours on a diamond cylinder at $\beta = 432$ for (a) KC = 1 and (b) KC = 3, at three different dimensionless times.

Comparing the values in Tables 2 and 3 shows that the drag coefficients for the rounded-corner cylinder are noticeably less than for the square-cornered cylinder. The inertia coefficients are slightly less for the rounded-corner cylinder case. We attribute these

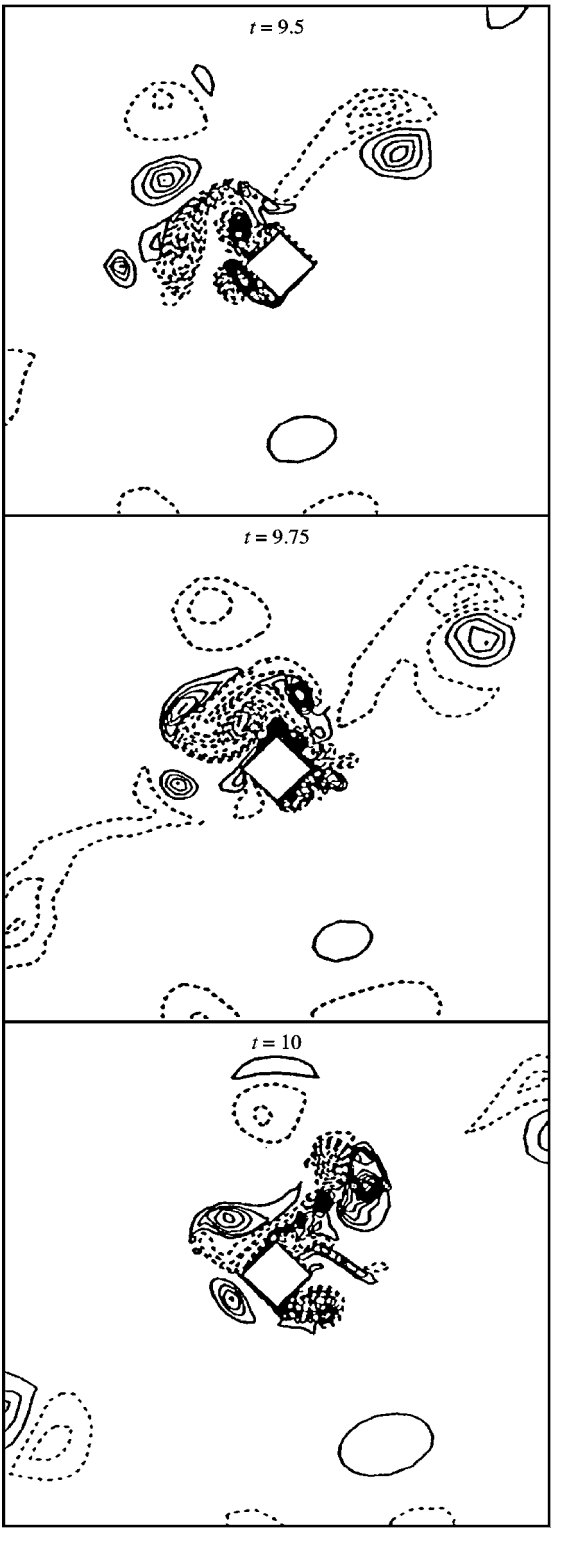

Figure 14. Near field of vorticity contours on a diamond cylinder at $\beta = 432$ and KC = 5 at three different dimensionless times.

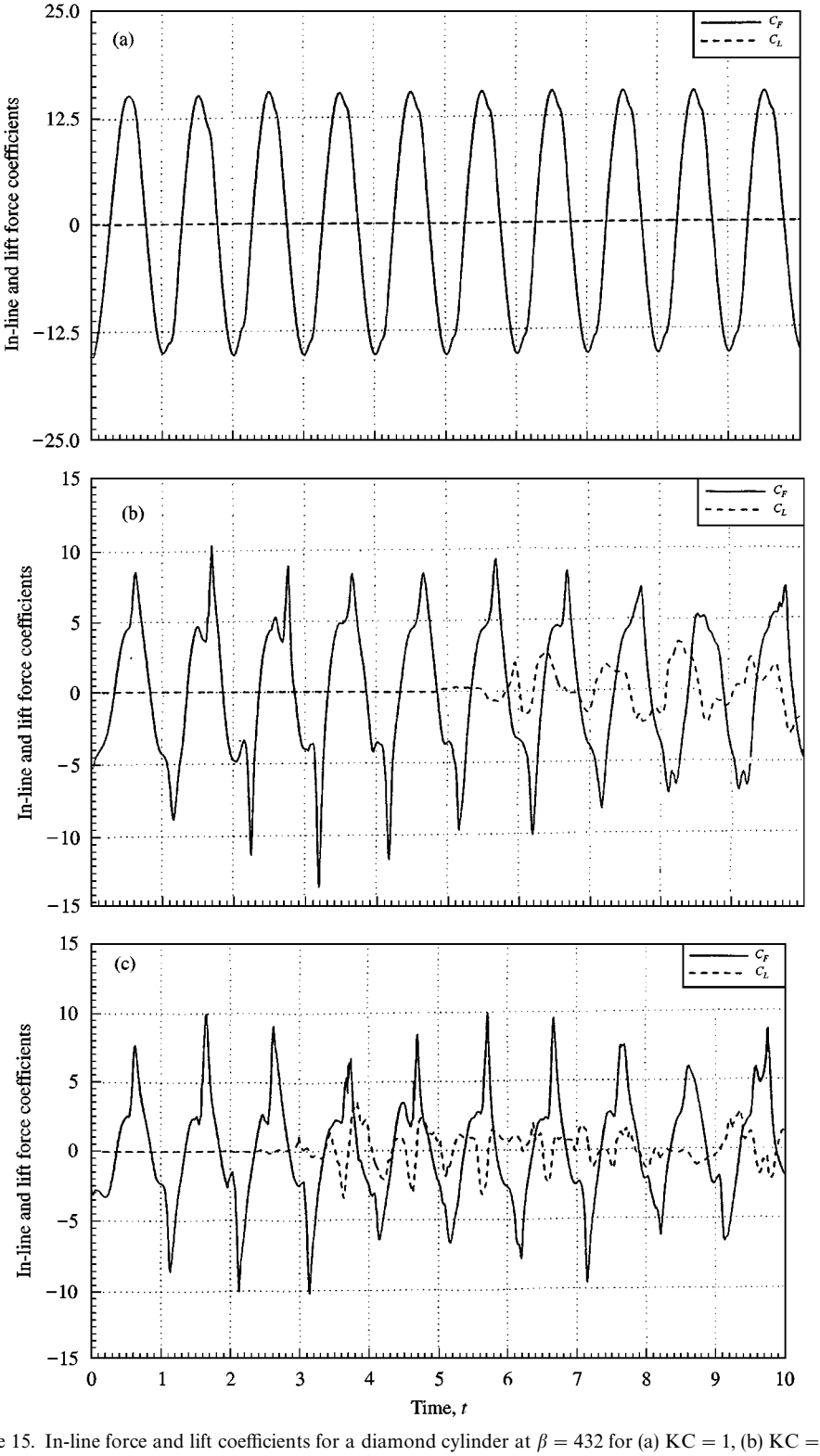

Figure 15. In-line force and lift coefficients for a diamond cylinder at $\beta = 432$ for (a) KC = 1, (b) KC = 3, and (c) KC = 5.

TABLE 4

Comparisons of the drag and inertia coefficients for oscillating flow past a diamond cylinder at $\beta = 432$

KC number	Present calculated C_D	Present calculated C_M	Scolan & Faltinsen calculated C_D	Scolan & Faltinsen calculated C_M	Bearman *et al.* experimental C_D	Bearman *et al.* experimental C_M
1	4·71	1·63	3·57	1·53	4·6	1·63
2	5·12	1·48	4·48	1·46	5·07*	1·63
3	5·58	1·41	4·03	1·33	5·67	1·72
4	4·84	1·43	3·77	1·42	5·28	1·68
5	4·78	1·66	3·19	1·37	4·81	1·69

*Interpolated.

differences to the fact that there is a slight difference between the well-defined separation point for the square-cornered cylinder case and the less well-defined separation point for the rounded-corner cylinder case.

5.3. DIAMOND CYLINDER

The computation of sinusoidally oscillating flow past a diamond cylinder with square corners was carried out for ten flow cycles on a 129×129 grid with local grid concentration at $\beta = 432$ and KC numbers ranging from 1 to 5. The minimum mesh size in the η direction in the physical plane is 0·01 while the minimum mesh size in the physical plane is 0·005 in the circumferential (ξ) direction with a hyperbolic tangentially distributed grid concentration near each of the four sharp corners. The maximum dimensionless distance between the centre of the cylinder and the outer boundary is 10. The time step Δt is 0·00025 at KC = 1, 0·0002 at KC = 2, 3 and 4, and 0·000125 at KC = 5.

The vorticity contours for $\beta = 432$ and KC = 1, 3, and 5 are shown in Figure 13 and 14 at dimensionless times of 9·5, 9·75, and 10 (through 10 cycles). The results at KC = 1 [Figure 13(a)] show a symmetric vortex pattern through ten cycles. The vorticity generated stays very close to the diamond cylinder except for a pair of symmetric wake vortices on each end that have evolved, due to induced velocity. For KC = 3, in Figure 13(b), the wake vortices, also shown in the tenth cycle, have become asymmetric well in advance of the tenth cycle [to be discussed for Figure 15(b)]. For KC = 5, in Figure 14, the wake vortices, also shown in the tenth cycle, have become quite disorganized due to the induced-velocity effects that have arisen from the wake asymmetry.

Figure 15 presents the variations of the in-line force coefficients C_F and the lift coefficients C_L at KC numbers from 1 to 5. At KC = 1, the variation of the in-line force coefficient shown in Figure 15, is basically smooth, periodic and symmetric with a little irregularity near each peak of the curve, and the lift coefficient is equal to zero. At KC = 3 [Figure 15(b)], asymmetric wake modes have developed to have strong effects on the in-line force coefficient with some fluctuation on the magnitude of each peak and a very sharp angle at each peak of the curve. Note the significant decrease in the value of the in-line force coefficient when the lift force develops, i.e., when the wake becomes asymmetric. At KC = 5 [Figure 15(c)], the variation of the in-line force and lift coefficients has strong fluctuation in the magnitude at each peak with irregular high frequency modes. The in-line force coefficient decreased in value somewhat when the lift developed, but not to the same extent as that

in Figure 15(b) for KC = 3. Note the earlier onset of asymmetry for the KC = 5 case over that for KC = 3.

The drag and inertia coefficients are calculated from the Morison equation through averaging the computed in-line force coefficient over the last five of the ten cycles at KC = 3 and 5, but without averaging at KC = 1. It is shown in Table 4 that the calculated drag and inertia coefficients at KC numbers from 1 to 5 agree very well with the experimental data obtained by Bearman *et al.* (1984). Comparisons of the calculated drag and inertia coefficients to the experimental values show the results in the present study agree more closely with experimental data than those in Scolan & Faltinsen (1994).

6. CONCLUSIONS

Numerical solutions of oscillating flow past a square cylinder, a diamond cylinder and a square cylinder with rounded corners are obtained from solving the 2-D Navier–Stokes equations in vorticity/stream-function variables on body-fitted coordinates. The second-order finite-difference approximations in both space and time are utilized to solve the unsteady flow problem with incorporation of a grid-generation technique and a third-order upwinding scheme in the nonlinear convective terms in the vorticity transport equation. A multigrid solver is used on the general elliptic partial differential equation with mixed derivatives and variable coefficients.

Numerical computations are carried out for an oscillating flow past a square cylinder at $\beta = 213$, a diamond cylinder at $\beta = 432$ and a square cylinder with rounded corners at $\beta = 172$ for KC numbers ranging from 1 to 5. It has been found that the calculated drag and inertia coefficients are in very good agreement with the experimental data obtained by Bearman *et al.* (1984) for oscillating flow past a square cylinder, a diamond cylinder and a square cylinder with rounded corners. The calculated drag and inertia coefficients are closer to the experimental data than those in several other computational studies. The behaviour of the inline force and lift coefficients is explained using vorticity contours that were obtained during the solution process. In conclusion, we feel that an accurate finite-difference solution is a better means of predicting forces on square bodies in an oscillating flow than a method that relies on a computational model such as the random vortex method.

ACKNOWLEDGEMENTS

The authors acknowledge the assistance of Prof. Richard Sanders in the Department of Mathematics at the University of Houston. Support for the first author was provided by the ERAP Program of the Department of Energy through the Texas Higher Education Coordinating Board. Some of the computer time was provided by the Pittsburgh Supercomputing Center.

References

Bearman, P. W., Graham, J. M. R., Obasaju, E. D. & Drossopoulos, G. M. 1984 The influence of corner radius on the forces experienced by cylindrical bluff bodies in oscillatory flow. *Applied Ocean Research* **6,** 83–89.

Davis, R. W. & Moore, E. F. 1982 A numerical study of vortex shedding from rectangles *Journal of Fluid Mechanics* **116,** 475–506.

Fletcher, C. A. J. & Srinivas, K. 1983 Stream function and vorticity revisited. *Computer Methods in Applied Mechanics and Engineering* **41**, 297–322.

Leonard, B. P. 1979 A stable and accurate convective modeling procedure based on quadratic upstream interpolation. *Computer Methods in Applied Mechanics and Engineering* **19,** 48–98.

MOFFATT, H. K. 1963 Viscous and resistive eddies near a sharp corner. *Journal of Fluid Mechanics* **18,** 1–18.

ROACHE, P. J. 1982 *Computational Fluid Dynamics*. Albuquerque, NM: Hermosa Press

SANDERS, R. 1992. Personal communication. Department of Mathematics, University of Houston.

SARPKAYA, T. & ISAACSON, M. 1981 *Mechanics of Wave Forces on Offshore Structures*. New York: Van Nostrand Reinhold.

SCOLAN, Y. M. & FALTINSEN, O. M. 1994 Numerical studies of separated flow from bodies with sharp corners by the vortex in cell method. *Journal of Fluids and Structures* **8,** 201–230.

SMITH, P. A. & STANSBY, P. K. 1991 Viscous oscillatory flows around cylindrical bodies at low Keulegan-Carpenter numbers using the vortex method. *Journal of Fluids and Structures*. **5,** 339–361.

TAMURA, T., OHTA, I. & KUWAHARA K. 1990 On the reliability of two-dimensional simulation for unsteady flows around a cylinder-type structure. *Journal of Wind Engineering and Industrial Aerodynamics* **35,** 275–298.